Article

Using Direct Current Potential Drop Technique to Estimate Fatigue Crack Growth Rates in Solid Bar Specimens under Environmental Assisted Fatigue in Simulated Pressurized Water Reactor Conditions

Sergio Arrieta [1,*], Francisco Javier Perosanz [2], Jose Miguel Barcala [3], Maria Luisa Ruiz [4] and Sergio Cicero [1]

[1] LADICIM, Laboratory of Materials Science and Engineering, Universidad de Cantabria, E.T.S. de Ingenieros de Caminos, Canales y Puertos, Av./Los Castros 44, 39005 Santander, Spain

[2] Combustion and Gasification Division, Energy Department, Centro de Investigaciones Energéticas, Medioambientales y Tecnológicas (CIEMAT), Avenida Complutense 40, 28040 Madrid, Spain

[3] Scientific Instrumentation Division, Technology Department, Centro de Investigaciones Energéticas, Medioambientales y Tecnológicas (CIEMAT), Avenida Complutense 40, 28040 Madrid, Spain

[4] Advanced Biofuels and Bioproducts Unit, Energy Department, Centro de Investigaciones Energéticas, Medioambientales y Tecnológicas (CIEMAT), Avenida Complutense 40, 28040 Madrid, Spain

[*] Correspondence: sergio.arrieta@unican.es

Abstract: The direct current potential drop (DCPD) technique may be used in crack propagation tests to measure the crack growth rate (CGR). Potential probes attached to the specimen allow the variation of the crack length to be estimated. In this research, the DCPD technique using one single potential probe was applied to solid bar specimens (i.e., without any initial notch or crack) subjected to low-cycle fatigue testing in a simulated pressurized water reactor (PWR) environment. This particular analysis had two associated difficulties, the first one being the fact that crack initiation sites are not known beforehand, and the second one consisting in the experimental difficulties and conditioning factors associated with the simulation of the PWR environment. Nine solid bar specimens were tested to fatigue failure under different strain amplitudes and frequencies, while also measuring the corresponding DCPD signal during the fatigue process. It was observed that the initiation of multiple cracks was detected by the DCPD measurements. Moreover, as fatigue continued, one of the cracks became dominant and progressed to cause the specimen failure. The DCPD technique allowed the average CGR of the dominant crack to be estimated. Finally, the obtained average CGRs were validated by comparing them with average CGRs derived from striation spacing measurements, obtained from scanning electron microscopy (SEM) and from literature values gathered in the NUREG/CR-6909 document.

Keywords: direct current potential drop; fatigue; environmental assisted fatigue; crack growth rate; pressurized water reactor

1. Introduction

The direct current potential drop (DCPD) technique is commonly used to measure the crack length in fatigue crack propagation tests [1,2]. Its use is particularly indicated for extensometric measurements in conductive materials tested in aggressive environments, where other conventional laboratory techniques cannot be used. Here, DCPD has been used in fatigue testing under simulated pressurized water reactor (PWR) conditions, at 300 °C and 150 bar, for the detection of crack initiation and growth.

The physical principle of this technique is based on Ohm's law and the corresponding evolution of the specimen resistance: the reduction of the cross-sectional area caused by the crack propagation is directly associated with an increase in the electrical resistance of the specimen. Moreover, the resulting potential drop is linked to a densification of the potential

field lines [3] and, therefore, both the specimen and the crack geometries play an important role [4–9].

Online monitoring of the potential drop signal enables a method for the estimation of crack growth rate (CGR) in environmental assisted fatigue tests to be developed, based on simple DCPD measurements.

During fatigue process, the crack development can be divided into three phases [10]:

- Phase 1: Crack nucleation. It comprises the number of fatigue cycles required to create a crack with a certain length (e.g., one grain) in a previously non-cracked material. Typically, fatigue crack nucleation may take place in two different conditions: material free of macroscopic defects, and material containing macroscopic defects (e.g., notches). In the first case, nucleation requires more fatigue cycles and represents a larger proportion of the total fatigue life. Micromechanisms of crack initiation have been widely analyzed and the reader is referred to the literature (e.g., [10,11]). When testing solid bars without macroscopic defects, fatigue crack initiation sites are located on the specimen surface, with a big proportion of the total fatigue life being consumed in the nucleation phase (80% can be taken as a reference [12]). Moreover, in solid specimens, the DCPD technique is able to detect this phase when multiple fatigue initiates occur simultaneously, but it is not possible to distinguish among the different initiation sites which crack will be the dominant one, propagating and causing the final failure.

- Phase 2: Crack propagation. This includes short crack growth and long crack growth. The first stage is governed by the material microstructure and corresponds to the number of load cycles required to grow a crack from the crack-nucleated grain until the crack is long enough to be modeled by bulk material properties, whereas the second one corresponds to a stage controlled by the bulk material properties and, in case of high cycle fatigue conditions, conventional linear elastic fracture mechanics (LEFM) is valid (e.g., Paris law [13]). In this second sub-phase, crack propagation is stable and continuous, the fatigue striations are generally well-defined, and the process is more easily analyzed by the DCPD technique. The crack progression marks may be observed with scanning electron microscopy (SEM) analysis. The striation pattern is a signal of microscopic plasticity and it is generated by blunting and re-sharpening of the crack-tip, during every load cycle (Laird's mechanism [14]). The striation spacing may also be used to estimate the local fatigue crack propagation rate (da/dN).

- Phase 3: Final failure. Fatigue crack propagation becomes unstable and the remaining cross-section can no longer resist the applied load, leading to final fracture or plastic collapse. This stage is not analyzed in the present research, as tests were stopped when a certain load drop was achieved.

DCPD has been widely used for crack propagation analysis in non-aggressive environments. This research, however, applied this technique for the analysis of both crack nucleation and crack propagation analyses in a PWR environment. To the knowledge of the authors, this is the first application in these particular conditions. The results obtained using DCPD have been validated by comparing them with the NUREG/CR-6176 [15] and NUREG/CR-6909 [16] expressions for corrosion fatigue in a PWR environment, and with the striation spacing measurements obtained from SEM images.

Section 2 presents the material being analyzed and the methods used in the research, Section 3 gathers the obtained results, Section 4 provides the corresponding discussion, and Section 5 outlines the main conclusions.

2. Materials and Methods

2.1. Material and Test Setup

Environmental assisted fatigue (EAF) tests were carried out on solid round bar specimens made of AISI 304L austenitic stainless steel. The specimen geometry and the chemical composition are shown in Figure 1a and Table 1, respectively. These kinds of specimens are not specifically designed and standardized to quantify the crack growth rate. Compact

tension (CT), center cracked tension (CCT), single edge notch tension (SENT), and single edge notch bend (SENB) specimens are usually used with this aim. In the solid round bar specimens, the gauge length was smooth, not containing any previous flaw or notch and meaning that the location of the crack initiation or nucleation site along the specimen gauge length was uncertain. Moreover, in this research, two different surface finishing conditions (polished and rough) were used.
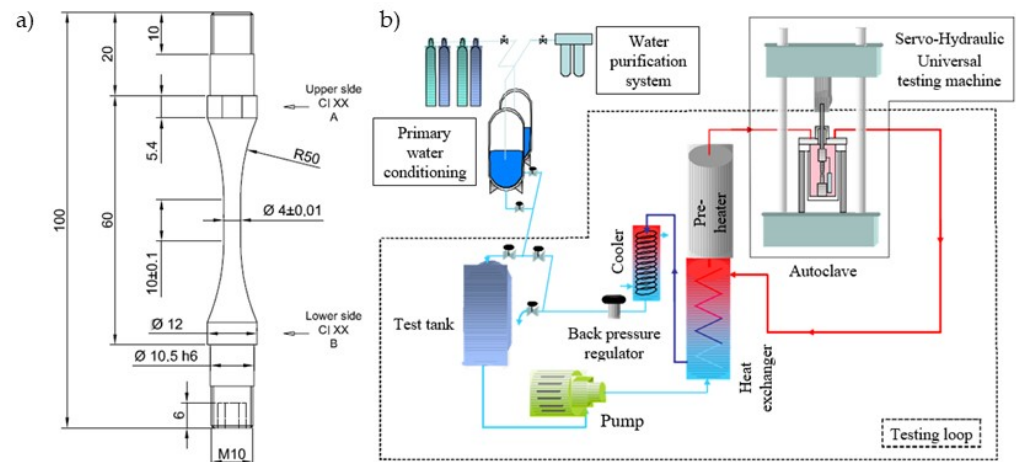
Figure 1. (**a**) Geometry of solid bar specimens (dimensions in mm); (**b**) schematic diagram of testing rig.

Table 1. Chemical composition of 304 L stainless steel (wt.%, Fe balance).

C	Cr	Cu	Mn	Mo	N	Ni	P	S	Si
0.029	18	0.02	1.86	0.04	0.056	10	0.029	0.004	0.37

Strain-controlled fatigue tests were performed under different loading conditions and frequencies (testing and environmental conditions shown in Tables 2 and 3, respectively). In all cases, the strain ratio, R, was fixed at −1. Uniaxial-strain-controlled fatigue testing in a PWR environment is not explicitly covered by any of the relevant fatigue standards. Therefore, the fatigue testing was performed following the indications of ASTM E606 [17] and ISO 12106 [18] standards, as strictly as could be expected in these very particular circumstances. A full description of the test conditions can be found in [19], in the frame of the INCEFA-PLUS Project.

Table 2. Some test parameters and resulting crack growth rates calculated using the DCPD signal and SEM fractography. R_a: arithmetic average roughness value [20]; R_t: total height of the roughness profile [20].

Test	R_a (μm)	R_t (μm)	Gauge Length (mm)	Diameter (mm)	Strain Amplitude (ε_m, %)	Rising Strain Rate (ε, %s^{-1})	Frequency (Hz)
CI6	1.632	14.470	10.0	3.79	0.60	0.01	0.0076
CI11	0.041	0.764	10.0	3.99	0.60	0.01	0.0076
CI12	0.028	0.351	10.0	3.99	0.23	0.01	0.0198
CI15	0.031	0.404	10.0	3.98	0.60	0.01	0.0076
CI16	0.041	0.490	10.0	4.00	0.60	0.01	0.0076
CI18	0.029	0.335	10.0	3.99	0.30	0.01	0.0152
CI19	2.015	17.895	10.0	3.75	0.60	0.01	0.0076
CI20	1.615	14.613	10.0	3.60	0.30	0.01	0.0152
CI22	1.948	17.077	10.0	3.65	0.23	0.01	0.0198

Table 3. Simulated PWR environment.

Parameter	Value
Temperature	300 °C ± 3 °C
Pressure	150 bar
Li content	2 ± 0.2 ppm as LiOH
B content	1000 ± 100 ppm as boric acid
Dissolved hydrogen	25 ± 5 cc(STP)H$_2$/kg (standard temperature and pressure (STP): 1 bar, 25 °C)
pH @300 °C	≈6.95
pH @25 °C	≈6.41
Conductivity @25 °C	≈30 μS/cm
Anionic contamination	<10 ppb
Oxygen	<5 ppb
Cationic contamination	<100 ppb
Total organic carbon (TOC)	<200 ppb

The device for carrying out the application of the load pattern to the fatigue specimen was a universal testing machine (MICROTEST Serie EFH) driven by a hydraulic power unit, fed by oil. The maximum work pressure was 150 bars. The test rig produced the necessary service conditions to carry out tests in a simulated PWR (see Table 3). The test rig scheme is shown in Figure 1b. The control of this fatigue testing setup was composed of two independent subsystems: the universal testing machine, with its own hydraulic unit; and the high temperature and pressure water loop, simulating primary water conditions.

The DCPD measurements were obtained using the Celians 3310/SUIV-FISSURE-5309 equipment. Two nickel wires with a 1 mm diameter were welded (capacitator discharge welding), above and below the specimen gauge length, providing the corresponding current inlet and outlet (see Figure 2). For the potential drop measurement, a constant current of 1 A was conducted through the specimens. The measured potential drop needed to be amplified before digitalizing by the acquisition system. In this case, the amplification was directly made by the Celians equipment. For every cycle, the current signal was measured, checking its evolution over time. In addition, a reference coupon made of the same material being tested was set next to the fatigue specimen, but not subjected to any loading. This sample eliminated small signal fluctuations caused by internal or external reasons (e.g., fluctuation of the electric current, variation of the temperature, changes in the resistivity of the material, etc.).
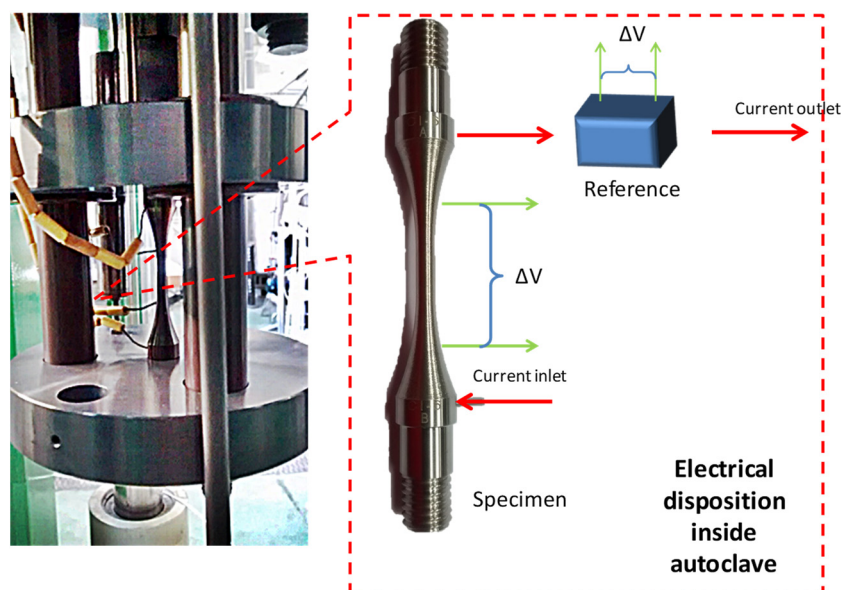
Figure 2. Experimental setup and schematic of the DCPD measurement system.

2.2. From DCPD Measurements to Crack Geometry

The potential drop technique allows an expression to be obtained that relates the voltage to the applied load pattern, the crack front advance and finally, when needed, the corresponding stress intensity factor. In the performed tests, the fatigue crack initiation site was located at the specimen surface and progressed towards the center of the tested specimen. The final crack length was physically measured once the EAF test was finished. Here, it is worth mentioning that specimens with multiple short cracks showed a significant scatter in the signal, whose origin can be attributed to the smaller length of the individual cracks, resulting in a lower potential drop and higher scatter of the potential drop measurement [6]. Additionally, the DCPD signal depended on the relative position of the crack initiation sites and the potential probes [6].

In the procedure, the crack geometry was correlated with the potential drop signal, obtaining an estimation of the crack length as a function of the cycle number. The DCPD signal was recorded using a frequency that allowed its evolution per cycle to be obtained, as shown in Figure 3. Changes in the electric current flowing across the specimen were directly related to the growth of the fatigue crack. Thus, from the measurement of the current variation it was possible to estimate the crack growth rate.
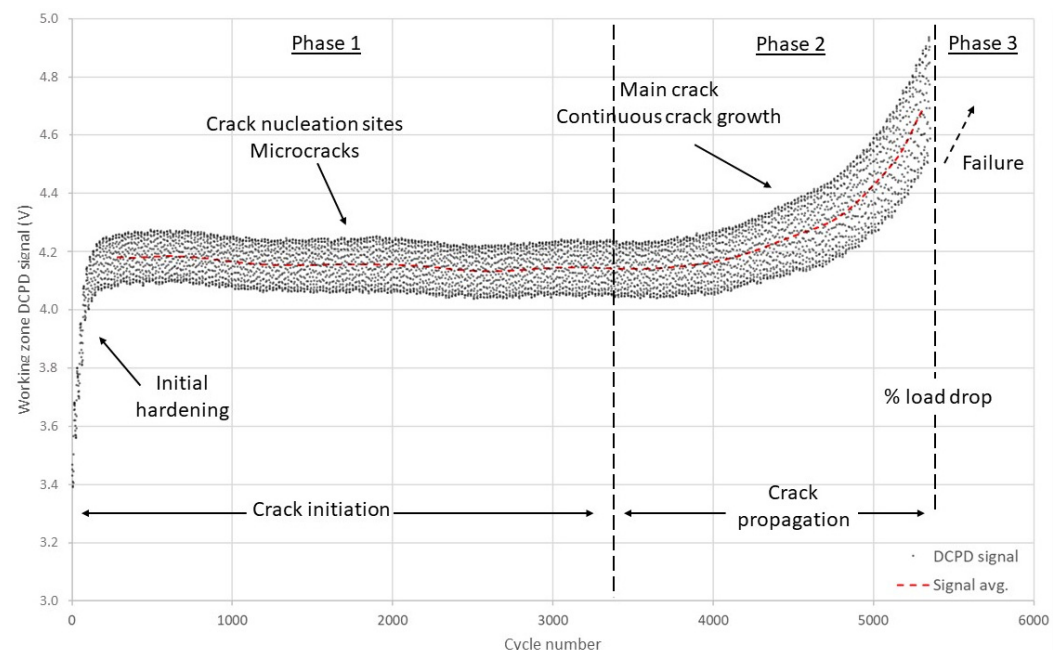
Figure 3. Evolution of DCPD signal in an EAF test and different crack regions.

With this aim, first, the following expression [21] was used:

$$\Delta \text{DCPD}_{\text{signal}} = \frac{1}{2} \left\{ \ln\left(\frac{V_{\text{test}}}{V_{\text{test0}}}\right) - \ln\left(\frac{V_{\text{ref}}}{V_{\text{ref0}}}\right) \right\} \tag{1}$$

where V_{test} is the potential measured in the gauge length throughout the test, V_{test0} is the initial value of V_{test} (t = 0), V_{ref} is the potential measured in the reference coupon throughout the test, and, V_{ref0} is the initial value of V_{ref} (t = 0).

The DCPD signal shown in Figure 3 identified the different stages of the crack development. At the beginning of the test (Phase 1), an increase could be observed in the signal due to the increase in the resistivity of the gauge length, which can be linked to the material hardening and microstructurally small cracks [16]. Later, the DCPD signal became stable. This plateau can be identified with crack nucleation, which may occur in different sites through the development of multiple micro-cracks. Once a crack reached sufficient length, crack growth rate accelerated (Phase 2, see equation (2)), and the specimen resistance

increased due to the reduction of the cross-section. The test was stopped before the full separation of the specimen (Phase 3), after achieving a certain percentage of load drop.

$$\frac{\text{dDCPD}_{\text{signal}}}{\text{dN}} > 0 \tag{2}$$

In order to apply Equation (2), the signal was smoothed by considering the middle-line (red dashed line in Figure 3). Then, the resulting line, including the stabilized part of Phase 1 and the whole Phase 2, was subsequently fitted using an exponential law.

As mentioned above, the DCPD signal depended on the relative position between the potential probe and the fatigue crack initiation sites [6]. In this research, this effect was not significant, as the distance between the probe inlet/outlet and the initiation sites was large enough to moderate the effect of the contour conditions in the crack initiation sections. In any case, when dealing with average CGRs (as it is the case in this work), the effect of such relative position should not be relevant, as both the crack initiation criterion and the final failure are not affected by it. In case of dealing with instantaneous CGRs, this issue would require special attention.

Next, with the aim of establishing a correlation between the measured DCPD signal and the extension of the crack, a geometrical model for the crack front during its propagation is required. The crack is assumed to be perpendicular to the applied load direction, and (in this work) it was defined by the intersection of two circumferences (see overlapping circles in Figure 4). Although the most common solution used in fracture mechanics analyses is the semi-elliptical crack front [22,23], here, based on the literature review and most of the fracture surfaces analyzed in the tested specimens, the crack front considered was that one defined by the intersection of two circumferences cutting each other perpendicularly [24–26] (see Figure 4). The final crack length considered during the process was that one for which the reduction of the resistant cross-section corresponded to a pre-defined percentage of load drop (e.g., 25%) [27].
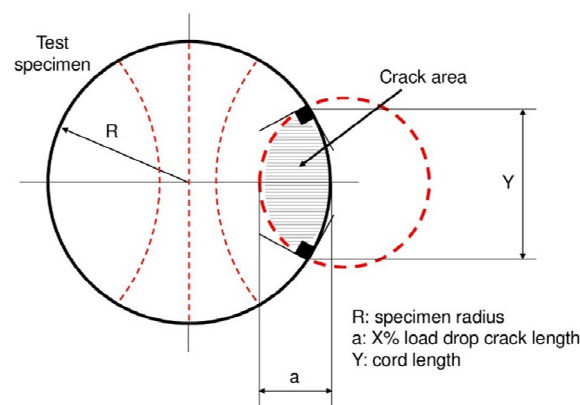
Figure 4. Overlapping circles model, adapted form [27], and development of the crack shape in cylindrical specimens.

The cracked area (S_c) was estimated as follows:

$$S_c = \frac{R^2}{\sin\left(\frac{Y}{2a}\right)} - \sqrt{s_1(s_1 - Y)(s_1 - Y)^2} + \frac{a^2}{\sin\left(\frac{Y}{2a}\right)} - \sqrt{s_2(s_2 - Y)(s_2 - a)^2}$$
$$s_1 = \frac{Y + 2R}{2}$$
$$s_2 = \frac{Y + 2a}{2} \tag{3}$$
$$Y = \frac{\sqrt{a^2(4R^2 - a^2)}}{R}$$

The resistant section (S_r) can be easily derived from Equation (4):

$$S_r = \pi R^2 - S_c \tag{4}$$

The estimation of the crack length using this geometrical model allows determining how the resistant section (S_r) of the specimen is reduced as a function of the crack length. As mentioned before, as the specimen section reduced, the electrical resistance increased.

Finally, in order to complete the crack growth model, it was necessary to measure the final crack length (a_f) reached by the crack during the EAF process in the PWR environment. Figure 5 shows the full facture surface of one of the tested samples. The cracked region was covered by the oxide film formed due to its exposure to simulated primary water during the fatigue tests, whereas the bright area was caused by a subsequent stress-controlled fatigue process in air (R > 0), performed until the specimen's final failure. The position of the most probable crack initiation site is highlighted by dotted red line.
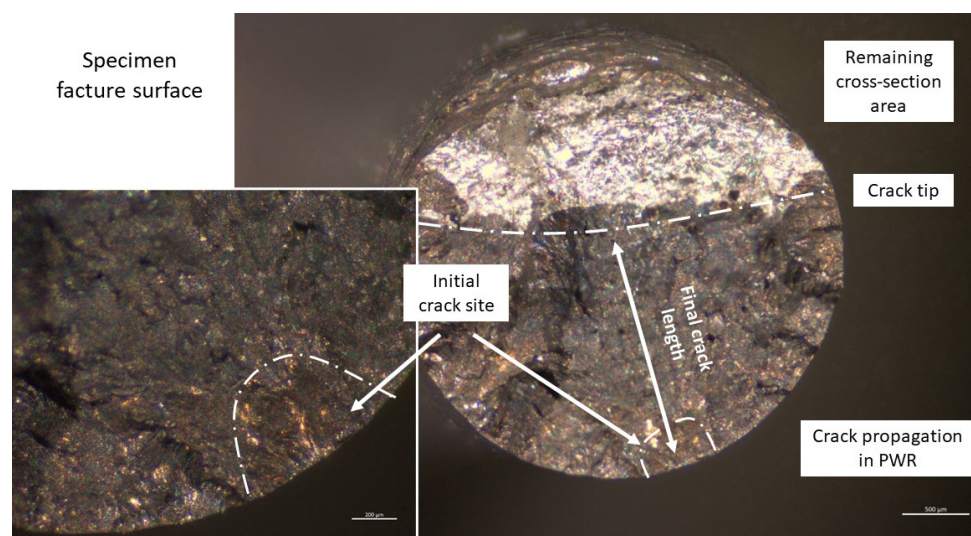

Figure 5. Specimen fracture surface after testing in a PWR environment.

Then, coupling the signal of the DCPD signal over time and the crack growth geometrical model allowed an estimation of the crack length as a function of the number of cycles (or test time) to be obtained, as shown in Figure 6. Fitting the $1/S_r$ curve up to the maximum crack length observed at the end of the test with the maximum value of the potential drop signal (ΔV), it was possible to derive a correlation between the DCPD signal and the instantaneous crack length. The complete steps are as follows:

1. Obtain the DCPD signal during the fatigue test. This allows the DCPD vs. time curve to be obtained. Given that the loading frequency is also known, the DCPD vs. number of cycles (N) curve may also be obtained.
2. Definition of geometrical model, which provides the relation between $1/S_r$ and the crack length through Equations (3) and (4)). The $1/S_r$ vs. crack length (a) curve is defined.
3. Measurement of the corresponding crack length at failure (a_f), for which the number of cycles is also known (N_f).
4. Definition of a_0 (i.e., 200 μm) and, obtainment of the corresponding number of cycles for crack initiation to be completed (N_0, see Figure 6).
5. Once (a_0, N_0) and (a_f, N_f) are defined, the obtainment of the average CGR is straightforward. If the whole crack length vs. number of cycles curve (e.g, see Figure 7 below) were needed, it would be necessary to proceed as in step d), but considering different crack sizes on the geometrical model.

The relation between the DCPD signal and the instantaneous crack require additional corrections in order to improve the corresponding accuracy (e.g., [5,6,28,29]). This way, it is possible to see the evolution of the crack over time and the instantaneous crack growth rate. The mentioned corrections require calibration processes that were not possible to accomplish in the aggressive particular experimental conditions covered in this work, so

the CGR analysis performed was focused on the average CGRs, not on instantaneous values. The calibration process was, thus, limited to measure the final crack length in the tested specimens and to assume a reasonable value for the crack length at initiation. In this sense, crack initiation was completed when Equation (2) was fulfilled (see Figure 3), and it was followed by crack propagation. The crack propagation was considered to start from an initial crack size of 200 μm (a_0, in agreement with [27,30]), which provides a value of the crack size from which stable growth occurs. This is consistent with the estimation of crack initiation and growth proposed in NUREG/CR-6909 [16].
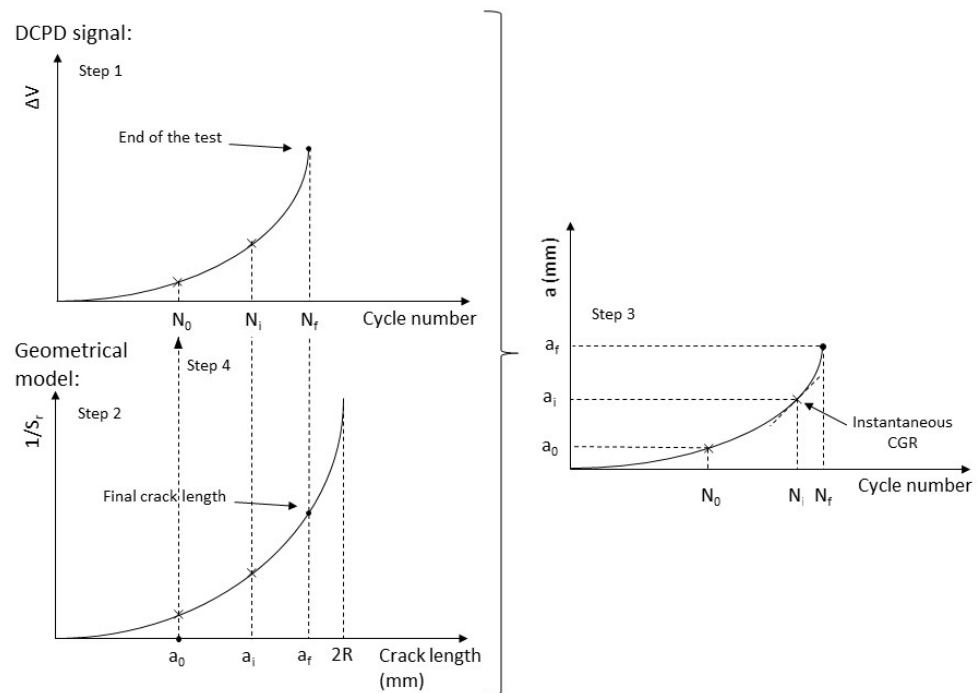
Figure 6. Estimation of the crack length when initiation is completed as function of the number of cycles (figure on the right) combining the DCPD signal (**top left**) and the applied geometrical model (**bottom left**).
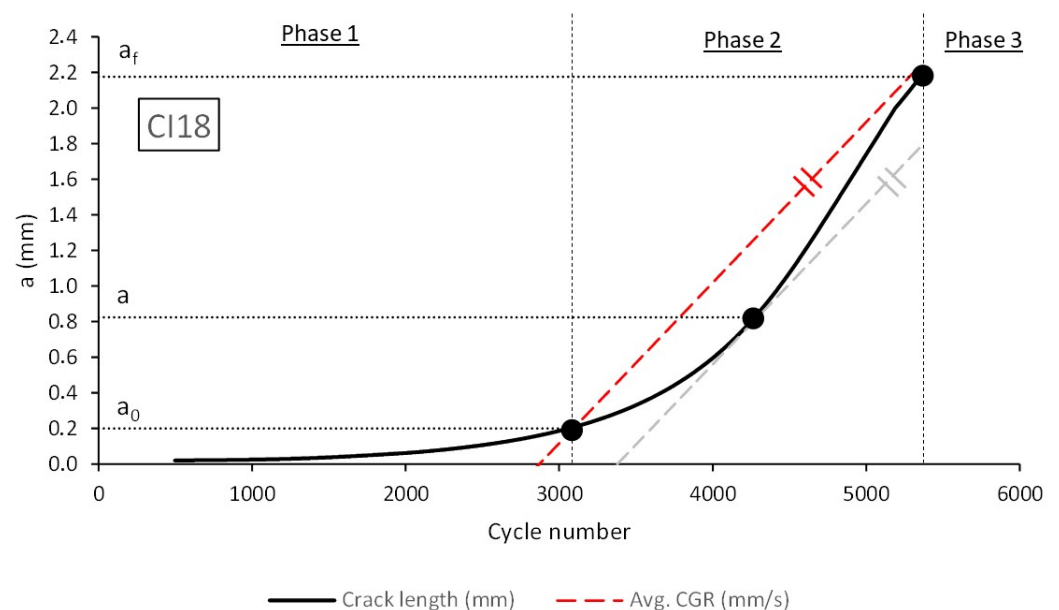
Figure 7. Estimation of crack size evolution derived from the DCPD signal and the crack geometrical model considered in this work.
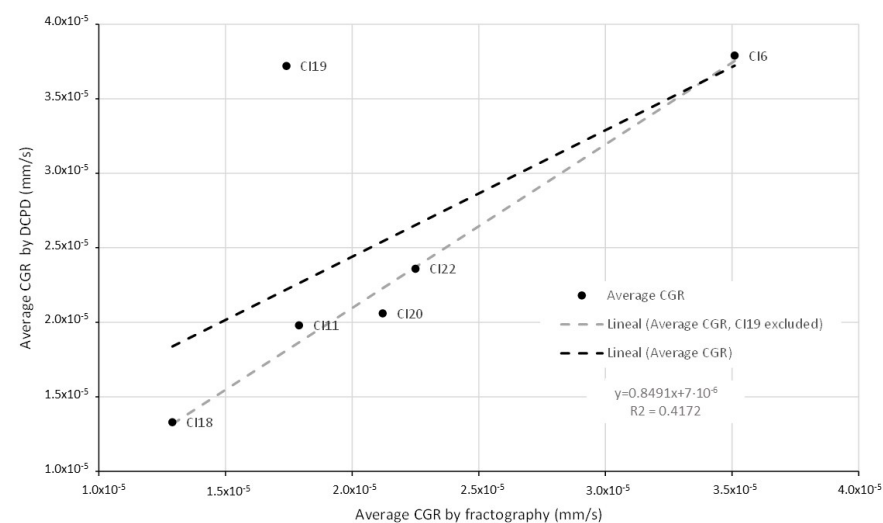
3. Results

Figure 7 shows an example of crack size evolution with the number of applied cycles (once initiation finishes), revealing how the methodology provides estimations of the crack propagation process.

Table 4 shows the crack growth rate results calculated from the DCPD signal, combining the potential drop and the crack growth model. These results are average values throughout the propagation process, obtained as shown in Figure 7 (dashed red line). It is possible to validate these predictions by comparing them to the CGR derived from the striation spacing (obtained from SEM images) and the loading frequency (see the results shown in Table 4 and Figure 8, and the fracture surface in Figure 9). This verification was not possible with some of the specimens on which SEM images did not provide clear reliable measurements of the striation spacing. For a given strain amplitude, and same strain rate (equal in all tests), the CGR varied moderately among the different specimens. However, the corresponding different measured values were all in the same order of magnitude, being consistent with the typical scatter obtained when measuring crack propagation rates. Furthermore, such differences in the measured CGRs of the different specimens occurred in both SEM measurements and DCPD signal measurements, demonstrating the consistency of the methodology proposed here. The effect of other variables, such as strain amplitude or surface roughness on the fatigue life, were not analyzed, as they have been analyzed in other works (e.g., [31–33]).

Table 4. Some test parameters and resulting crack growth rates calculated using the DCPD signal and SEM fractography. N_{25}: fatigue life (cycles), defined at 25% load drop.

Test	Strain Amplitude (%)	Load Drop (%)	Final Crack Length (mm)	Average CGR (DCPD) (mm/s)	Average CGR (Fractography) (mm/s)	N_{25} (Cycles)
CI6	0.60	100	3.321	3.79×10^{-5}	3.51×10^{-5}	673
CI11	0.60	31	1.907	1.98×10^{-5}	1.79×10^{-5}	1414
CI12	0.23	36	2.422	1.14×10^{-5}	-	11,018
CI15	0.60	35	3.734	1.64×10^{-5}	-	1311
CI16	0.60	50	2.760	1.81×10^{-5}	-	1447
CI18	0.30	32	2.175	1.33×10^{-5}	1.29×10^{-5}	5241
CI19	0.60	39	2.366	3.72×10^{-5}	1.74×10^{-5}	1004
CI20	0.30	35	2.033	2.06×10^{-5}	2.12×10^{-5}	3326
CI22	0.23	51	2.727	2.36×10^{-5}	2.25×10^{-5}	5800

Figure 8. Correlation between DCPD estimation and measurement of striations spacing for the different specimens.
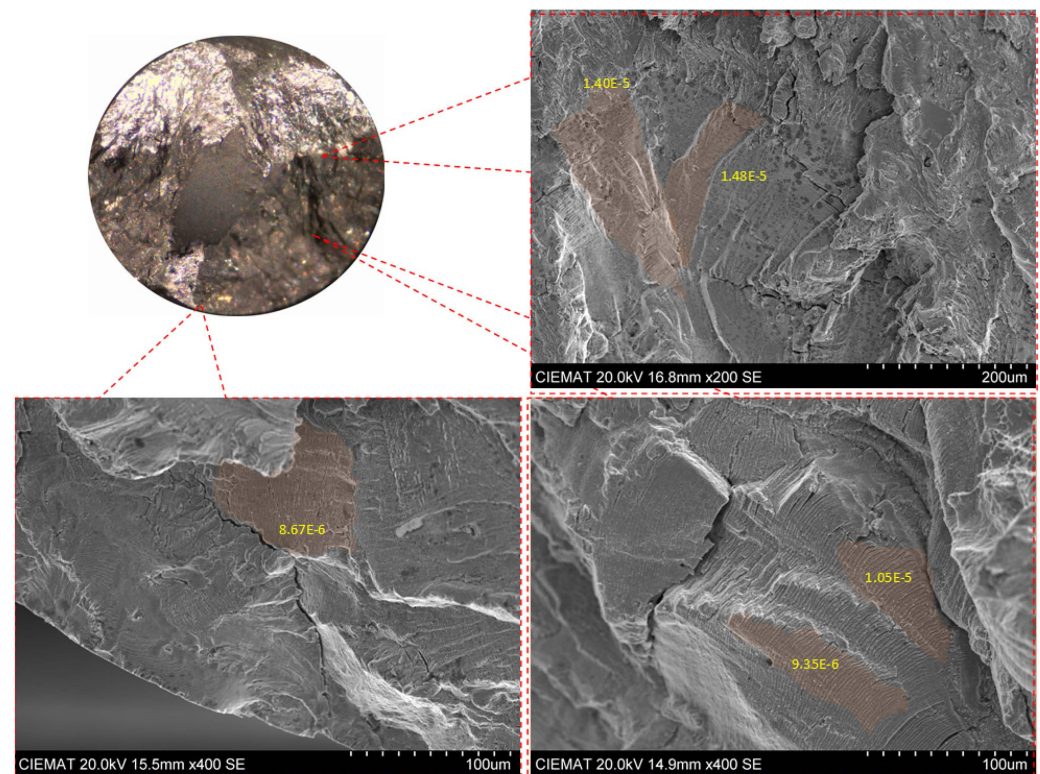
Figure 9. SEM images of fracture surfaces, measurement of striation spacing, and resulting crack growth rates (CGR (mm/s)).

Figure 8 shows the correlation between the CGR obtained from DCPD estimations and by striation spacing measurement. For the sake of consistency, crack growth rates derived from striation spacing also represent average values derived from approximately equispaced measurements taken along the crack propagation surface. The final average values were directly obtained by measuring individual values of a high number of points along the fatigue surface, basically in most of the striations observed from the initiation site to the last position of the crack front during the fatigue test. This number was high enough to ensure a robust representative result, not sensitive to the final number of points being considered. This procedure, which is not ideal, was followed due to the fact that striation spacing was not always measurable along the crack propagation path. Precisely, those specimens in Table 4 with no CGRs derived from fractography (CI12, CI15 and CI16) correspond to those situations in which the fatigue surfaces were particularly damaged and, thus, both the number of measurable striation spacings was very low and the final results were not consistent.

The correlation between both values seemed good in most cases, although a weaker result appeared for the CI19 specimen, still in the same order of magnitude. It would be necessary to perform more verifications in future test programs to check that this discrepancy was not recurrent. It is important to note that if such a result (CI19 specimen) is not considered, the correlation between the two measurements would be very high, as also shown in Figure 8.

The resulting instantaneous propagation rates, estimated from the SEM fractography, were between 9.5×10^{-6} mm/s and 1.5×10^{-5} mm/s (see Figure 9). These values are reasonable taking into account the areas where they have been measured and the values reported in the literature [34,35], and led to the average CGR values shown in Table 4.

The CGR results derived from DCPD and SEM fractography were also compared with the fatigue crack growth rates in a PWR environment proposed in NUREG/CR-6909 [16] (see Figure 10) for austenitic stainless steels in a PWR environment. The expressions for

CGR in the air (CGR$_{air}$, Equation (5)) and CGR in the environment (CGR$_{env}$, Equation (6)), were both derived from [8,9]:

$$CGR_{air} = 3.43 \cdot 10^{-12} S(R) \Delta K^{3.3} / T_r \tag{5}$$

$$CGR_{env} = CGR_{air} + 4.5 \cdot 10^{-5} (CGR_{air})^{0.5} \tag{6}$$

where S(R) is a function of the load ratio (in these tests, S(R) = 1.0), ΔK is the range of the stress intensity factor, and T_r is the rise time of the loading waveform.
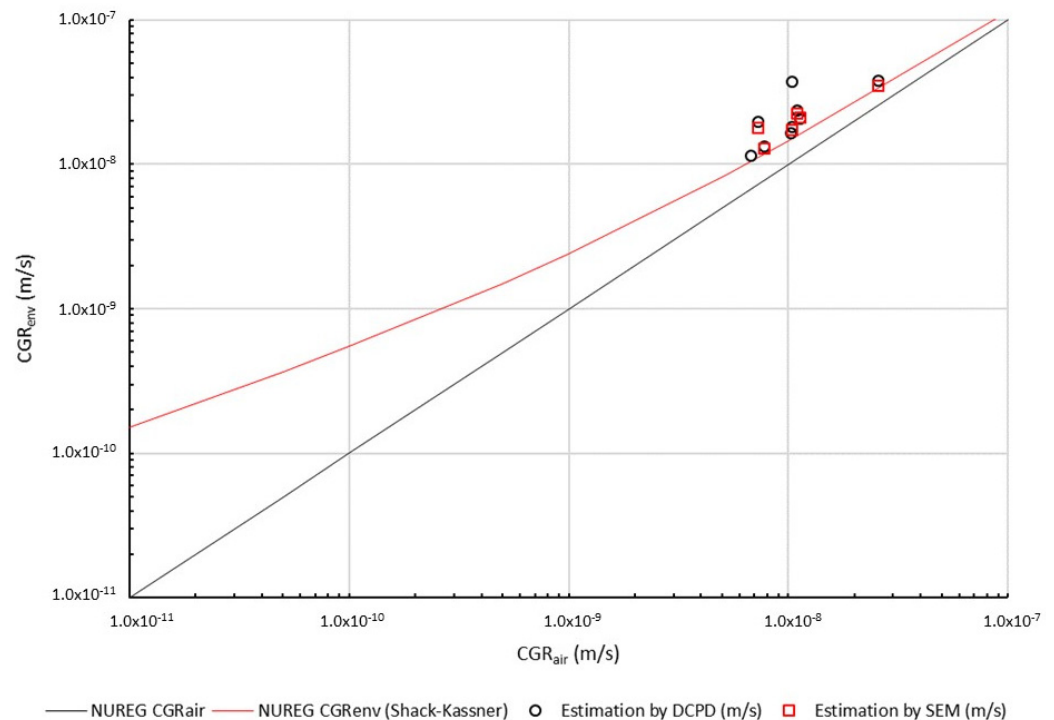
Figure 10. CGRs (obtained by DCPD and SEM fractography) compared with the curves proposed in NUREG/CR-6909 (air and PWR environment).

To compare the experimental CGRs obtained from DCPD and fractography with the estimations provided by NUREG/CR-6909, although test conditions are elastoplastic, a general approximation to the stress intensity factor (Equation (7)) was made, following [36,37].

$$\Delta K = F \Delta \sigma \sqrt{\pi a} \tag{7}$$

where $\Delta \sigma$ is the stress range, a is the crack length, and F is a geometrical factor that depends on both the crack geometry and the component (specimen) geometry. For cylindrical bars under tension and circumferential crack front, Equation (8), was selected [24]:

$$F = 0.92 \frac{\pi}{2} \sqrt{\frac{\tan \frac{\pi a}{2D}}{\frac{\pi a}{2D}}} \frac{1}{\cos \frac{\pi a}{2D}} \left[0.752 + 2.02 \frac{a}{D} + 0.37 \left(1 - \sin \frac{\pi a}{2D} \right)^3 \right] \tag{8}$$

where a is the crack length and D is the diameter of the specimen.

Given that this analysis focused on average crack growth rates, the crack length (a) used to estimate the stress intensity factor (ΔK) was the one corresponding to the same slope (i.e., instantaneous CGR) as that providing the average CGR, which was derived from the final crack length (a_f), measured on the crack surface, and the initial crack length (a_0) (see Figure 7, dashed gray line, leading to 0.82 mm in the example). In other words, the crack length considered in Equation (8), a, is that one corresponding to an instantaneous CGR equal to the average CGR.

Figure 10 shows the estimations of CGRs obtained in the analyzed cylindrical specimens and in a PWR environment when using the DCPD approach and the SEM fractographies, and compares them to those predicted by NUREG/CR-6909 (red line for PWR environment, black line for air conditions) [8,9].

Some observations about these verifications can be made:

(a) There is a good correlation between the values measured by fractography and those estimated by potential drop.

(b) The estimated values (points) are above the curve fitted by Shack and Kassner (originally developed in NUREG/CR-6176 [15]), which corresponds to oxygenated environments. This agrees with the fact that the CGR in environments with low oxygen content (PWR) increases when compared with the CGR in environments with higher oxygen content (boiling water reactor, BWR) [38].

4. Discussion

The work described above has shown that it is possible, by using the potential drop technique, to estimate average crack growth rates (CGRs) in solid bar specimens tested in a PWR environment. These particular testing conditions are associated with specific issues, such as the uncertainty about the location of crack initiation sites and the proper experimental difficulties linked to the simulation of harsh environments. The proposed experimental procedure and an analytical model allowed an easy and fast determination of the average fatigue crack growth rate.

The specimen geometry used in this research, cylindrical solid specimens without initial notch or pre-crack, is commonly used for determining fatigue life (S-N curves), but not for measuring crack growth rates. The described procedure makes it possible to increase the versatility of the information that this type of tests can provide.

The proposed methodology measures the DCPD signal along the fatigue test, determines the actual final crack length on the fatigue specimen after failure, assumes a given crack length at initiation (200 μm), and couples the DCPD signal with a geometrical model of the crack.

The average CGRs estimated with the proposed procedure have been compared to those derived from the measures of striation spacing, observing reasonably good correlations, and suggesting the suitability of the approach for the combination of material and environment tested here. The estimations have been also compared with the NUREG/CR-6909 expressions, again providing reasonable agreement between them.

The approach also allows estimation of the evolution of the crack depth during the fatigue process, but the corresponding accuracy must be validated in future research. It would require comparing the slope at different points of the curve, shown in graphs such as Figure 7, with the corresponding exact locations (in terms of crack depth) in the fatigue fracture surface. Unfortunately, this was not feasible in this research, as fatigue striations did not appear continuously and consistently along the fatigue surface, due to the strain control conditions of the tests and the application of negative strain values that damaged the fatigue surface.

Common issues in fatigue tests, such as multiple crack initiation sites or different crack propagation paths, can occur. These unwanted, but inevitable, issues have an influence on the DCPD signal and can distort the determination of the crack growth rate.

The crack front profile can take different shapes, due to microstructure or geometry, so this point should be addressed in the model of crack growth [4,8]. This question could be further analyzed using finite element analysis.

5. Conclusions

This work introduces a procedure for using the DCPD technique to estimate the average fatigue crack growth rate in solid bar specimens tested in a PWR environment, without previous notch or pre-cracking processes.

The proposed methodology measures the DCPD signal along the fatigue test, determines the actual final crack length on the fatigue specimen after failure, assumes a given crack length at initiation (e.g., 200 μm) and couples the DCPD signal with a geometrical model of the crack. In this way, both the evolution of the crack size with the number of cycles and the average value of the crack growth rate (CGR) in a PWR can been obtained. The average crack growth rate estimations have been compared to those derived from the fatigue striation spacing measured in the fracture surface and to the CGR values suggested in NUREG/CR-6176 and NUREG/CR-6909, providing reasonable accuracy in both cases.

Thus, it has been proven that it is possible to obtain practical estimations of average CGRs in a PWR environment.

Author Contributions: Conceptualization, F.J.P. and S.A.; methodology, F.J.P. and S.A.; software, F.J.P. and J.M.B.; validation, F.J.P. and S.A.; formal analysis, S.A. and F.J.P.; investigation, S.A., F.J.P., J.M.B., M.L.R. and S.C.; data curation, F.J.P. and S.A.; writing—original draft preparation, S.A. and F.J.P.; writing—review and editing, S.A., F.J.P., J.M.B., M.L.R. and S.C.; project administration, F.J.P.; funding acquisition, F.J.P. All authors have read and agreed to the published version of the manuscript.

Data Availability Statement: Not applicable.

Conflicts of Interest: The authors declare no conflict of interest. The funders had no role in the design of the study; in the collection, analyses, or interpretation of data; in the writing of the manuscript, or in the decision to publish the results.

References

1. Bauschke, H.-M.; Schwalbe, K.-H. Measurement of the Depth of Surface Cracks Using the Direct Current Potential Drop Method. *Mater. Werkst.* **1985**, *16*, 156–165. [CrossRef]
2. *ASTM E647-00*; Standard Test Method for Measurement of Fatigue Crack Growth Rates. ASTM International: West Conshohocken, PA, USA, 2000.
3. Ritchie, R.O.; Garrett, G.G.; Knott, J.P. Crack-Growth Monitoring: Optimisation of the Electrical Potential Technique Using an Analogue Method. *Int. J. Fract. Mech.* **1971**, *7*, 462. [CrossRef]
4. Doremus, L.; Nadot, Y.; Henaff, G.; Mary, C.; Pierret, S. Calibration of the Potential Drop Method for Monitoring Small Crack Growth from Surface Anomalies—Crack Front Marking Technique and Finite Element Simulations. *Int. J. Fatigue* **2015**, *70*, 178–185. [CrossRef]
5. Campagnolo, A.; Meneghetti, G.; Berto, F.; Tanaka, K. Calibration of the Potential Drop Method by Means of Electric FE Analyses and Experimental Validation for a Range of Crack Shapes. *Fatigue Fract. Eng. Mater. Struct.* **2018**, *41*, 2272–2287. [CrossRef]
6. Hartweg, M.; Bär, J. Analysis of the Crack Location in Notched Steel Bars with a Multiple DC Potential Drop Measurement. *Procedia Struct. Integr.* **2019**, *17*, 254–261. [CrossRef]
7. Bär, J. Crack Detection and Crack Length Measurement with the DC Potential Drop Method–Possibilities, Challenges and New Developments. *Appl. Sci.* **2020**, *10*, 8559. [CrossRef]
8. Vecchiato, L.; Campagnolo, A.; Meneghetti, G. Numerical Calibration and Experimental Validation of the Direct Current Potential Drop (DCPD) Method for Fracture Mechanics Fatigue Testing of Single-Edge-Crack Round Bars. *Int. J. Fatigue* **2021**, *150*, 106316. [CrossRef]
9. Bär, J.; Nahbein, M. Investigation of Crack Formation and Propagation in AA7475 Using Multiple Potential Drop Measurement. *Procedia Struct. Integr.* **2022**, *37*, 336–343. [CrossRef]
10. ASM International. *ASM Handbook, Volume 19: Fatigue and Fracture*; ASM International: West Conshohocken, PA, USA, 1997; ISBN 0-87170-385-8.
11. Suresh, S. *Fatigue of Materials*; Cambridge University Press: Cambridge, UK, 1998; ISBN 9780521570466.
12. Deng, G.J.; Tu, S.T.; Wang, Q.Q.; Zhang, X.C.; Xuan, F.Z. Small Fatigue Crack Growth Mechanisms of 304 Stainless Steel under Different Stress Levels. *Int. J. Fatigue* **2014**, *64*, 14–21. [CrossRef]
13. Paris, P.C.; Erdogan, F. A Critical Analysis of Crack Propagation Laws. *J. Basic Eng. Trans. Am. Soc. Mech. Eng.* **1963**, *15*, 528–534. [CrossRef]
14. Laird, C.; Smith, G.C. Crack Propagation in High Stress Fatigue. *Philos. Mag. A J. Theor. Exp. Appl. Phys.* **1962**, *7*, 847–857. [CrossRef]

15. Shack, W.J.; Kassner, T.F.; Technology, E. NUREG/CR-6176; ANL-94/1. In *Review of Environmental Effects on Fatigue Crack Growth of Austenitic Stainless Steels*; Nuclear Regulatory Commission: North Bethesda, MD, USA, 1994.

16. Chopra, O.K.; Stevens, G.L. *NUREG/CR-6909, Rev.1. Effect of LWR Water Environments on the Fatigue Life of Reactor Materials, Final Report*; United States Nuclear Regulatory Commission: North Bethesda, MD, USA, 2018.

17. *E606/E606M-12*; ASTM Standard Test Method for Strain-Controlled Fatigue Testing. ASTM International: West Conshohocken, PA, USA, 2004. [CrossRef]

18. *ISO/FDIS 12106:2016(E)*; ISO Metallic Materials—Fatigue Testing—Axial-Strain-Controlled Method. International Organization for Standardization: Geneva, Switzerland, 2016.

19. INCEFA-PLUS Consortium; Arrieta, S.; Austin, T.; Bruchhausen, M.; Chitty, W.-J.; Cicero, R.; Cicero, S.; Cuvilliez, S.; De Baglion, L.; Dundulis, G.; et al. *INCEFA-PLUS Findings on Environmental Fatigue*; Cicero, S., Arrieta, S., Procopio, I., Eds.; INCEFA-PLUS Project: Santander, Spain, 2020; ISBN 978-84-09-24496-6.

20. *ISO 4287:1997*; Geometrical Product Specifications (GPS)—Surface Texture: Profile Method—Terms, Definitions and Surface Texture Parameters. International Organization for Standardization: Geneva, Switzerland, 1997; Volume 1998, pp. 1997–1998.

21. Toloczko, M.B.; Olszta, M.J.; Zhai, Z.; Bruemmer, S.M. Stress Corrosion Crack Initiation Measurements of Alloy 600 in PWR Primary Water. In Proceedings of the 17th International Conference on Environmental Degradation of Materials in Nuclear Power Sytems—Water Reactors, Ottawa, ON, Canada, 9–13 August 2015; pp. 1–20.

22. Carpinteri, A. Stress-Intensity Factors for Semi-Elliptical Surface Cracks under Tension or Bending. *Eng. Fract. Mech.* **1991**, *38*, 327–334. [CrossRef]

23. Carpinteri, A. Shape Change of Surface Cracks in Round Bars under Cyclic Axial Loading. *Int. J. Fatigue* **1993**, *15*, 21–26. [CrossRef]

24. Levan, A.; Royer, J. Part-Circular Surface Cracks in Round Bars under Tension, Bending and Twisting. *Int. J. Fract.* **1993**, *61*, 71–99. [CrossRef]

25. James, L.A.; Mills, W.J. Review and Synthesis of Stress Intensity Factor Solutions Applicable to Cracks in Bolts. *Eng. Fract. Mech.* **1988**, *30*, 641–654. [CrossRef]

26. Lin, X.B.; Smith, R.A. Shape Evolution of Surface Cracks in Fatigued Round Bars with a Semicircular Circumferential Notch. *Int. J. Fatigue* **1999**, *21*, 965–973. [CrossRef]

27. Gosselin, S.; Nunez, D.; Esselman, T.; Cluever, J. *Development of Fatigue Usage Life and Gradient Factors*; Technical Report 3002014121; EPRI: Palo Alto, CA, USA, 2018; p. 84.

28. Johnson, H. Calibrating the Electric Potential for Studying Slow Crack Growth. *Mater. Res. Stand.* **1965**, *5*, 442–445.

29. Hicks, M.A.; Pickard, A.C. A Comparison of Theoretical and Experimental Methods of Calibrating the Electrical Potential Drop Technique for Crack Length Determination. *Int. J. Fract.* **1982**, *20*, 91–101. [CrossRef]

30. Chopra, O.K.; Shack, W.J.; Muscara, J. Mechanism of Fatigue Crack Initiation in Austenitic Stainless Steelsin Light Water Reactor Environments. In Proceedings of the 17th International Conference on Structural Mechanics in Reactor Technology (SMiRT17), International Association for Structural Mechanics in Reactor Technology, Prague, Czech Republic, 17–22 August 2003; p. 8.

31. Mottershead, K.; Bruchhausen, M.; Cicero, S.; Cuvilliez, S. Incefa-Plus: Increasing Safety in NPPs by Covering Gaps in Environmental Fatigue Assessment; PVP2020-21220. *Am. Soc. Mech. Eng. Press. Vessel. Pip. Div. PVP* **2020**, *1*, 1–5.

32. Bruchhausen, M.; Mclennan, A.; Cicero, R.; Huotilainen, C.; Mottershead, K.; Le Roux, J.-C.; Vankeerberghen, M. Incefa-Plus Project: Review of the Test Programme; PVP2020-21377. *Am. Soc. Mech. Eng. Press. Vessel. Pip. Div. PVP* **2020**, *1*, 1–10.

33. Bruchhausen, M.; Dundulis, G.; McLennan, A.; Arrieta, S.; Austin, T.; Cicero, R.; Chitty, W.-J.; Doremus, L.; Ernestova, M.; Grybenas, A.; et al. Characterization of Austenitic Stainless Steels with Regard to Environmentally Assisted Fatigue in Simulated Light Water Reactor Conditions. *Metals* **2021**, *11*, 307. [CrossRef]

34. Tice, D.; Platts, N.; Rigby, K.; Stairmand, J.; Swan, D. Influence of PWR Primary Coolant Environment on Corrosion Fatigue Crack Growth of Austenitic Stainless Steel. In Proceedings of the ASME 2005 Pressure Vessels and Piping Conference, Denver, CO, USA, 17–21 July 2005; Volume 1: Codes and Standards. ASMEDC: New York, NY, USA, 2005; pp. 193–205.

35. Vlčková, I.; Jonšta, P.; Jonšta, Z.; Váňová, P.; Kulová, T. Corrosion Fatigue of Austenitic Stainless Steels for Nuclear Power Engineering. *Metals* **2016**, *6*, 319. [CrossRef]

36. Al Laham, S. *Stress Intensity Factor and Limit Load Handbook*; British Energy Generation Ltd.: Glasgow, UK, 1999.

37. Raju, I.S.; Newman, J.C., Jr. *Stress-Intensity Factors for Circumferential Surface Cracks in Pipes and Rods under Tension and Bending Loads*; NASA: Hampton, VA, USA, 1985.

38. Mills, W.J. Accelerated and Retarded Corrosion Fatigue Crack Growth Rates for 304 Stainless Steel in an Elevated Temperature Aqeous Environment. In Proceedings of the 16th Internation Conference on Environmental Degradation of Materials in Nuclear Power Systems-Water Reactors, Ottawa, ON, Canada, 11–15 August 2013.